

Numerical approximations of a norm-preserving gradient flow and applications to an optimal partition problem

This article has been downloaded from IOPscience. Please scroll down to see the full text article.

2009 Nonlinearity 22 67

(<http://iopscience.iop.org/0951-7715/22/1/005>)

[The Table of Contents](#) and [more related content](#) is available

Download details:

IP Address: 137.132.123.69

The article was downloaded on 11/08/2009 at 04:22

Please note that [terms and conditions apply](#).

Numerical approximations of a norm-preserving gradient flow and applications to an optimal partition problem*

Qiang Du¹ and Fanghua Lin²

¹ Department of Mathematics, Pennsylvania State University, University Park, PA 16802, USA

² Courant Institute, New York University, New York, NY 10012, USA

E-mail: qdu@math.psu.edu and linfh@cims.nyu.edu

Received 8 September 2008, in final form 27 October 2008

Published 2 December 2008

Online at stacks.iop.org/Non/22/67

Recommended by A L Bertozzi

Abstract

We present and analyse numerical approximations of a norm-preserving gradient flow and consider applications to an optimal eigenvalue partition problem. We consider various discretizations and demonstrate that many of the properties shared by the continuous counterpart can be preserved at the discrete level. The numerical algorithms are then used to study the nonlinear and non-local interfacial dynamics associated with the optimal partition.

Mathematics Subject Classification: 65M12, 35K50, 65P40, 49R50

(Some figures in this article are in colour only in the electronic version)

1. Introduction

Given a bounded and smooth geometric domain $\Omega \subset \mathbb{R}^d$, a positive integer m and a small positive parameter ϵ , the following energy functional has been introduced in [CL2] for any vector-valued function $u = \{u_j\} \in [H_0^1(\Omega)]^m$:

$$E^\epsilon(u) = \int_{\Omega} (|\nabla u|^2 + 2F_\epsilon(u)) \, dx, \quad (1)$$

where F_ϵ is an interaction potential of the form

$$F_\epsilon(u) = \frac{1}{\epsilon^2} \sum_{i=1}^m \sum_{j<i} u_i^2 u_j^2. \quad (2)$$

* This paper is published as part of a collection in honour of Todd Dupont's 65th birthday.

The problem of minimizing the functional E^ϵ over the set of $u \in [H_0^1(\Omega)]^m$ satisfying the normalization condition

$$\int_{\Omega} |u_j|^2 \, d\mathbf{x} = 1, \quad j = 1, \dots, m \quad (3)$$

has received much attention due to its connection to a number of applications such as the study of multicomponent Bose–Einstein condensates [B, BaD, CLLL], and the study of optimal eigenvalue partition problems [CL, CL1, CL2]. This constrained minimization problem also has a corresponding norm-preserving gradient dynamics [CL1], that is, the following nonlinear parabolic system:

$$\begin{cases} \partial_t u_j^\epsilon - \Delta u_j^\epsilon = \lambda_j^\epsilon(t) u_j^\epsilon - F_{\epsilon,j}(u^\epsilon) & \text{in } \Omega \times \mathbb{R}_+, \quad 1 \leq j \leq m, \\ u^\epsilon(t, \mathbf{x}) = 0 & \text{on } \partial\Omega \times \mathbb{R}_+, \\ \int_{\Omega} |u_j^\epsilon|^2 \, d\mathbf{x} = 1, & \text{for } j = 1, \dots, m, \quad t > 0 \end{cases} \quad (4)$$

along with the initial condition

$$u^\epsilon(0, \mathbf{x}) = g(\mathbf{x}) \in H_0^1(\Omega, \Xi), \quad \text{with } \int_{\Omega} g_j^2(\mathbf{x}) \, d\mathbf{x} = 1, \quad 1 \leq j \leq m. \quad (5)$$

Here, $F_{\epsilon,j}$ denotes the partial derivative with respect to the j th variable (for $1 \leq j \leq m$) and Ξ is a singular subset in \mathbb{R}^m :

$$\Xi = \left\{ y \in \mathbb{R}^m \mid \sum_{j=1}^m \sum_{k < j} y_j^2 y_k^2 = 0, \text{ and } y_k \geq 0 \text{ for } 1 \leq k \leq m \right\}. \quad (6)$$

Nonlinear dynamics governed by equations of the type (4) are of practical interest by themselves. In the study of BECs, with various general interaction potentials, they may represent the imaginary time integrations which lead to the ground state [AD, BaD]. In population biology and ecology, they may lead to spatial segregation of competing species [BDa, CTV1, CTV2, CTV3, CTV4]. In materials science, they may also be tied to the diffuse interface models for the widely studied microstructure evolution [C].

The main focus of this paper is to present some algorithms for the approximation of the above norm-preserving gradient flows along with their rigorous mathematical analysis and their applications to a nonlinear optimal partition problem. Some nice features of the numerical schemes are established, in the same spirit as those shared by the original dynamic equations. Both fully implicit nonlinear schemes and semi-implicit splitting schemes are presented. Connections to the existing studies of an optimal eigenvalue partition problem and other related domain partitions and interfacial dynamics are made to link the analysis and computation with interesting applications. Numerical simulations and their implications are presented. The results not only illustrate the rich nonlinear dynamics governed by the norm-preserving gradient flows and the non-local features associated with the optimal partition problem but also motivate future analytical and computational investigations.

The rest of the paper is organized as follows. In section 2, we recall the background of the problem and discuss various relevant mathematical formulations. In section 3, we present several algorithms for the approximation of the norm-preserving gradient flow and provide the relevant numerical analysis. Numerical results are given in section 4 and applications to the nonlinear interfacial dynamics associated with the optimal eigenvalue partition problems are considered there also. Finally, some additional comments are made in section 5.

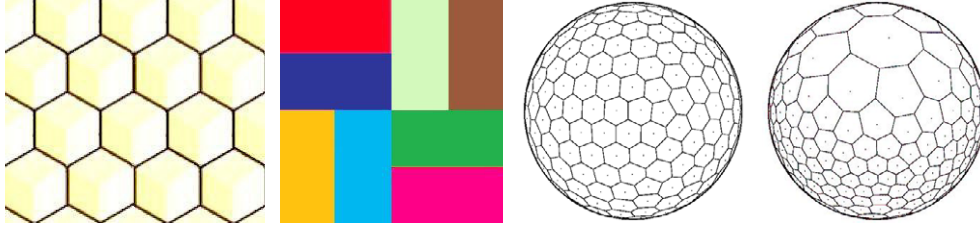


Figure 1. Honeycomb structure (left), rectangular tiling (centre) and CVTs of a spherical surface with both uniform and non-uniform densities (right).

2. Background

Given a bounded and smooth domain Ω in \mathbb{R}^d , and a positive integer $m \geq 1$, a partition (also called tessellation) of the domain Ω is defined as a collection of mutually disjoint subsets $\{\Omega_i\}_{i=1}^m$ of Ω such that $\bar{\Omega} = \bigcup_{j=1}^m \bar{\Omega}_j$; see figure 1 for some examples.

Domain partition and tessellation are widely used in many scientific and engineering applications. Often some optimal partition may be desired, with the optimality defined with respect to various objective functionals, some of which may involve simple calculus while others may require substantial computation. A popular two dimensional example is the honeycomb (hexagonal) structure (see the left picture in figure 1), while some regular and uniform tilings also appear very often (second picture in figure 1). We have studied a popular partition criterion related to a simple energy:

$$E_{\text{cvt}}(\{\Omega_i\}) = \sum_i \int_{\Omega_i} \rho(\mathbf{x}) |\mathbf{x} - \mathbf{y}_i|^2 \, d\mathbf{x} \quad (7)$$

for some non-negative density ρ and points $\{\mathbf{y}_i \in \Omega\}$ [DFG]. The minimizer of E_{cvt} leads to the concept of centroidal Voronoi tessellations whose interior boundaries are formed by piecewise line segments for the Euclidean metric (or geodesic curves for CVTs on a sphere, see the two pictures on the right in figure 1). In practice, there are substantially more complex partitions defined by other optimization properties. In this work, we are interested in an example given by the energy functional:

$$\Lambda^0(\{\Omega_i\}) = \sum_{j=1}^m \lambda_1(\Omega_j), \quad (8)$$

where $\lambda_1(\Omega_j)$ is the first Dirichlet eigenvalue of the Laplacian Δ on Ω_j with zero Dirichlet boundary condition on $\partial\Omega_j$. Such an optimal eigenvalue partition problem has been studied by many authors (see [CL] and the references therein). Not only is an optimal partition desirable, the evolution from an arbitrary partition to an optimal one through a gradient flow of the energy may also reveal rich dynamics.

As noted in [CL1], one preliminary difficulty associated with the minimization of the functional (8) and associated gradient flow is to define a class of admissible subsets of Ω so that one can properly define the meaning of the Dirichlet eigenvalues on such sets. Furthermore, it is also a subtle issue to define a suitable topology on the space of these admissible sets. In [CL], the optimal partition problem associated with the functional (8) is shown to be equivalent to a constrained harmonic mapping problem

$$\min \left\{ \int_{\Omega} |\nabla v|^2 \, d\mathbf{x} \mid v \in H_0^1(\Omega, \Xi), \int_{\Omega} v_j^2 \, d\mathbf{x} = 1, \, j = 1, \dots, m \right\}, \quad (9)$$

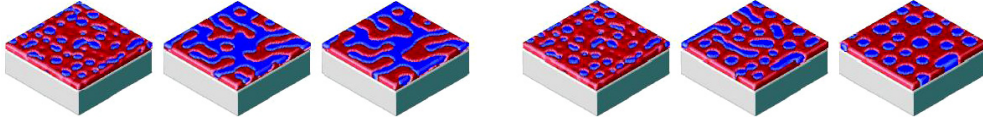


Figure 2. Microstructure evolutions with different elastic moduli may favour either networks (left) or particles (right) [YHCD].

where Ξ is given by (6). Besides the connection to (8), the energy functionals (9) and the regularized version (1) are often directly associated with other minimization problems such as the free energy minimization in multicomponent BECs [CLLL]. In [CL], it is shown that there is an energy minimizing map $u \in H_0^1(\Omega, \Xi)$ with a unit L^2 norm such that u is Lipschitz continuous on $\bar{\Omega}$, and that the open sets $\Omega_j = \{\mathbf{x} \in \Omega \mid u_j > 0\}$ for $j = 1, \dots, m$ form a partition of Ω in the sense that $\bar{\Omega} = \cup_{j=1}^m \bar{\Omega}_j$ with $\bar{\Omega}_j \setminus \Omega_j$ are $C^{2,\alpha}$ in Ω away from a relatively closed subset of Ω of Hausdorff dimension no more than $d - 2$ for $j = 1, \dots, m$. Moreover, the energy E in (8) is minimized by the admissible partition $A_1 = \bar{\Omega}_1, A_2 = \bar{\Omega}_2 \setminus A_1, \dots, A_m = \bar{\Omega}_m \setminus \cup_{j=1}^{m-1} A_j$. Conversely, if A_1, A_2, \dots, A_m is an admissible partition that minimizes E in (8), then let u_j be the normalized eigenfunction on A_j :

$$\begin{aligned} \Delta u_j + \lambda_1(\Omega_j)u_j &= 0 && \text{in } A_j, \\ u_j &= 0 && \text{on } \bar{\Omega} \setminus A_j, \end{aligned}$$

where $u \in [\tilde{H}_0^1(\Omega)]^m$ with

$$[\tilde{H}_0^1(\Omega)]^m = \left\{ u \in [H_0^1(\Omega)]^m \mid \int_{\Omega} |u_j|^2 dx = 1, \quad j = 1, \dots, m. \right\}. \quad (10)$$

It has been shown in [CL1] that $u = \{u_j\} : \Omega \rightarrow \Xi$ minimizes the functional in (9). In [CL2], a constrained gradient flow of the problem (9) was introduced with the time dependent solution $u(t, \cdot)$ belonging to Ξ , and each component satisfying (3). The nonlinear system (4) was introduced as a natural relaxation of such dynamics. Such techniques have been widely used in recent years in various contexts, and they can also be classified as *diffuse interface* or *phase field* formulations of the limiting *sharp interface* problems.

Besides the various possible practical applications that have been alluded to earlier, the time dependent problem (4) also leads to many mathematically interesting questions such as the regularity of underlying moving free interfaces and their geometric evolutions. The motion of the interface is governed by an energy (objective) functional (8) which is not directly defined through a local parametrization of the interfacial boundary but rather through the computation in the bulk domain in a non-local fashion. Such problems are not unique, in fact, they are intimately related to the study of microstructure evolution widely studied in materials sciences. In fact, while many of the existing studies focus on the case of the interface governed by interfacial energies such as the surface tension or bending elastic energies [DLW, DLRW] or surface diffusion [BBW], it is important to point out that non-local long-range interaction energies, such as electric dipole–dipole interactions and electrostatic energies, have also played important roles. Moreover, the nucleation process and the interfacial evolution in elastic materials (see an example in figure 2) are greatly influenced by the bulk properties such as the anisotropic elastic energy [C, ZCD]. Thus, the gradient dynamics of (8) may be viewed as another extreme case where the interfacial tension is ignored and only the bulk non-local energy is accounted for. The studies of such dynamics will naturally shed light on the understanding of more general interfacial dynamics and microstructure evolution.

One of the main difficulties in dealing with the gradient dynamics of (8) directly is the use of the singular set Ξ . To overcome this obstacle, system (5) is studied in [CL2] as a regularization

scheme. This is in the same spirit as the diffuse interface or phase field description of the free or moving interface problems [C]. In the limit $\epsilon \rightarrow 0$, it has been shown that [CL2], in the appropriate sense, the solutions of system (5) converges to the original constrained gradient dynamics of the harmonic mappings (8). Furthermore, (5) provides a good computational approach to investigate the underlying dynamics effectively which we demonstrate in this paper.

Before we continue to the numerical approximations, we recall that it has been proved in [CL2] that

$$\lambda_j^\epsilon(t) = \int_{\Omega} \left(|\nabla u_j^\epsilon|^2 + u_j^\epsilon F_{\epsilon,j}(u^\epsilon) \right) dx \quad (11)$$

and

$$E^\epsilon(u^\epsilon(t, \mathbf{x})) \leq \sum_{j=1}^m \lambda_j^\epsilon(t) = E^\epsilon(u^\epsilon(t, \mathbf{x})) + \int_{\Omega} 2F_\epsilon(u^\epsilon) dx, \quad (12)$$

with $E^\epsilon(u^\epsilon(t, \mathbf{x}))$ being a monotone decreasing function of $t \geq 0$. The above properties lead to the existence of a unique global strong solution $u^\epsilon \in L^\infty(R_+, [H_0^1(\Omega)]^m)$ of the norm-preserving gradient flow system (4) for each positive ϵ . Moreover, they are useful in the analysis of the *sharp interface* limit as $\epsilon \rightarrow 0$. For instance, it is shown in [CL2] that for any given $t > s > 0$, one has

$$\int_s^t \int_{\Omega} F_\epsilon(u^\epsilon) dx dt \rightarrow 0 \quad \text{as } \epsilon \rightarrow 0 \quad (13)$$

so that for small ϵ the difference between the energy and the sum of the Lagrange multipliers is nearly the same. Furthermore, the limit of u^ϵ becomes a suitable weak solution of the gradient flow for the constrained harmonic mapping problem.

For convenience, we hereby introduce the following functionals:

$$\begin{cases} S^\epsilon(u^\epsilon(t, \mathbf{x})) = \int_{\Omega} F_\epsilon(u^\epsilon(t, \mathbf{x})) dx, \\ \Lambda^\epsilon(u^\epsilon(t, \mathbf{x})) = E^\epsilon(u^\epsilon(t, \mathbf{x})) + 2S^\epsilon(u^\epsilon(t, \mathbf{x})). \end{cases} \quad (14)$$

As the norm-preserving and energy decreasing properties are important for the study of underlying dynamics, the preservation of those features becomes important in the numerical computation.

3. Discrete approximations

Here, we present some numerical algorithms to approximate the norm-preserving gradient flow (4). An emphasis on the time discretization is made in light of the need for long time integrations. Details on the spatial discretizations can be found in the next section.

We now set up some notation. For convenience, we often drop the explicit dependence of the solutions on the parameter ϵ if there is no ambiguity. Let us choose a time sequence $0 = t_0 < t_1 < t_2 < \dots < t_n < \dots$ with $\Delta t_n = t_{n+1} - t_n > 0$ and $\tau = \max_{n \geq 0} \Delta t_n$. The numerical approximation of $u = \{u_j(t, \mathbf{x})\}$ at $t = t_n$ is denoted by $u^n = \{u_j^n = u_j^n(\mathbf{x})\}$. We let $\delta_t u^n = (u^{n+1} - u^n) / \Delta t_n$ be the time difference, and $u^0 = g$ be the initial condition.

3.1. A convergent fully implicit nonlinear scheme

We first define a fully implicit Euler scheme for (4) which is a generalization of a similar method proposed in [AD, D].

$$\begin{cases} \delta_t u_j^n = \Delta u_j^{n+1} + \lambda_j^{n+1} u_j^{n+1} - F_{\epsilon, j}(u^{n+1}) & \text{in } \Omega \times \mathbb{R}_+, \\ u_j^n = 0 & \text{on } \partial\Omega \times \mathbb{R}_+, \\ \int_{\Omega} |u_j^{n+1}|^2 \, d\mathbf{x} = 1, & 1 \leq j \leq m, \, t > 0. \end{cases} \quad (15)$$

In (15), the Lagrange multiplier λ_j^{n+1} can also be viewed as the eigenvalues of a coupled nonlinear eigenvalue problem. The existence and stability of the above fully implicit scheme is assured by the following lemma.

Lemma 3.1. *For any $\Delta t_n > 0$, and $u^n \in [\bar{H}_0^1(\Omega)]^m$, a solution to the following constrained variational problem:*

$$\min \left\{ E^\epsilon(u) + \frac{1}{\Delta t_n} \int_{\Omega} |u - u^n|^2 \, d\mathbf{x} \mid u \in [\bar{H}_0^1(\Omega)]^m \right\} \quad (16)$$

always exists and it satisfies equation (15). Moreover, for sufficiently small Δt_n , the global minimizer is unique.

Proof. Due to the non-negativity of the objective functional, we easily get the existence of a minimizing sequence $\{u_k\}_{k=1}^\infty$ in $[\bar{H}_0^1(\Omega)]^m$ whose objective functional values are uniformly bounded from the above by the objective functional value at u^n . Moreover, it is easy to show that the objective functional is coercive, which thus implies that $\{u_k\}$ is uniformly bounded in $[\bar{H}_0^1(\Omega)]^m$.

Since the objective functional is also weakly lower-semi continuous in $[H_0^1(\Omega)]^m$ and the set $[\bar{H}_0^1(\Omega)]^m$ is closed for a weakly convergent sequence in $[H_0^1(\Omega)]^m$, we get that there exists a weak limit of the $\{u_k\}$ which is a minimizer of the variational problem in $[\bar{H}_0^1(\Omega)]^m$.

A direct calculation of the Euler–Lagrange equation shows that all the minimizers must satisfy equation (15). Moreover, the minimizers are all bounded in $[H_0^1(\Omega)]^m$. Since the nonlinear term $\nabla F_\epsilon(v)$ is locally Lipschitz in $[L^2(\Omega)]^m$ for v bounded in $[H_0^1(\Omega)]^m$, it is then straightforward to show that, for Δt_n small enough (depending only on the norm of u^n in $[H_0^1(\Omega)]^m$), the global minimizer is unique. \square

The equivalence between (15) and (16) is very useful in the analysis of the fully implicit schemes for nonlinear parabolic systems which has been frequently used in the literature, see for instance [D2].

A consequence of the above lemma is the following *a priori* estimate:

Lemma 3.2. *The solution of (15) satisfies for any $n \geq 1$ and any $j = 1, \dots, m$ that*

$$\int_{\Omega} |u_j^n|^2 \, d\mathbf{x} = 1, \quad (17)$$

$$E^\epsilon(u^{n+1}) + \frac{1}{\Delta t_n} \int_{\Omega} |u^{n+1} - u^n|^2 \, d\mathbf{x} \leq E^\epsilon(u^n), \quad (18)$$

$$\lambda_j^n = \int_{\Omega} [|\nabla u_j^{n+1}|^2 + u_j^{n+1} F_{\epsilon, j}(u^{n+1})] \, d\mathbf{x} + \frac{1}{\Delta t_n} (1 - \int_{\Omega} u_j^{n+1} u_j^n \, d\mathbf{x}). \quad (19)$$

Proof. The normalization condition (17) is part of the constraint. Since u^n satisfies the constraint, its objective functional value gives an upper bound to the value at the minimizer (or the solution u^{n+1}). The equation for the Lagrange multiplier can be derived directly by multiplying, in component-wise form, the first equation of (15) by the corresponding components of u^{n+1} . \square

Equation (19) provides a formula for the computation of the Lagrange multipliers. Moreover, summing over j , we get

$$\sum_j \lambda_j^n = E^\epsilon(u^{n+1}) + 2 \int_\Omega F_\epsilon(u^{n+1}) \, dx + \frac{1}{2\Delta t_n} \|u^{n+1} - u^n\|^2, \quad (20)$$

which is a discrete analogue of (12). Based on the *a priori* bound (18), we immediately get a uniform upper bound for the Lagrange multipliers.

In addition, taking the sum n of (18), we get

$$E^\epsilon(u^{N+1}) + \sum_{n=0}^N \Delta t_n \int_\Omega |\delta_t u^n|^2 \, dx \leq E^\epsilon(g). \quad (21)$$

Now, if we let $u_\tau = u_\tau(t)$ be the piecewise linear interpolation of $\{u^n\}$ in time at the time steps $\{t_n\}$, then, we immediately get the uniform bound of u_τ in $L^\infty(R_+, [\bar{H}_0^1(\Omega)]^m) \cap H^1(R_+, [\bar{H}_0^1(\Omega)]^m) \cap L_{\text{loc}}^2(R_+, [H^2(\Omega)]^m)$ with respect to τ . Thus, adopting the techniques given [CL2], we have the following theorem.

Theorem 3.1. *Given the conditions specified earlier, as $\tau \rightarrow 0$, u_τ converges weakly (or weakly *) to the unique global solution u of (4) in $L^\infty(R_+, [\bar{H}_0^1(\Omega)]^m) \cap H^1(R_+, [\bar{H}_0^1(\Omega)]^m) \cap L_{\text{loc}}^2(R_+, [H^2(\Omega)]^m)$.*

Proof. The argument follows from standard lines. First, the uniform bounds allow the extraction of a weakly (or weakly *) convergent subsequence of u_{τ_k} in $L^\infty(R_+, [\bar{H}_0^1(\Omega)]^m) \cap H^1(R_+, [\bar{H}_0^1(\Omega)]^m) \cap L_{\text{loc}}^2(R_+, [H^2(\Omega)]^m)$ as $\tau_k \rightarrow 0$. Then it is easy to verify that the weak limit must satisfy the suitable weak form of (4). The *a priori* bounds and the regularity argument then imply that the weak limit is in fact the unique global solution of (4). The uniqueness of the limit in turn leads to the convergence of the whole sequence u_τ as $\tau \rightarrow 0$. \square

We note, moreover, that the *a priori* bounds on u_τ do not depend on ϵ since $E^\epsilon(g)$ is independent of ϵ , so at least the weak convergence in ϵ can also be expected. The full discretization in both space and time can be considered similarly.

In addition, the discrete scheme still preserves the non-negativity of the solutions with suitably restricted time steps.

Lemma 3.3. *The solution of (15) satisfies for any $n \geq 1$ and any $j = 1, \dots, m$ that, for small enough Δt_n (depending only on the initial condition g),*

$$u_j^n(x) \geq 0, \quad \text{a.e. in } \Omega. \quad (22)$$

Proof. We proceed with induction. Since the conclusion is satisfied at $n = 0$ for the initial conditions, with the assumption that

$$u_j^k(x) \geq 0, \quad \text{a.e. in } \Omega.$$

for any $k \leq n$, we now consider $\{u_j^{n+1}\}$. By (15), we get

$$\left(\frac{1}{\Delta t_n} - \lambda_j^n + \frac{2}{\epsilon^2} \sum_{i \neq j} (u_i^{n+1})^2 \right) u_j^{n+1} - \Delta u_j^{n+1} = \frac{1}{\Delta t_n} u_j^n.$$

Because λ_j^n is uniformly bounded, if Δt_n is small enough such that $\Delta t_n \lambda_j^n < 1$, then

$$\frac{1}{\Delta t_n} - \lambda_j^n + \frac{2}{\epsilon^2} \sum_{i \neq j} (u_i^{n+1})^2 \geq 0, \quad \text{a.e. in } \Omega.$$

By the maximum principle for the second order elliptic equations and the induction hypothesis we easily get for any j ,

$$u_j^{n+1}(x) \geq 0, \quad \text{a.e. in } \Omega.$$

This proves the non-negativity of $\{u_j^n\}$ for any $n \geq 0$. \square

We note that to study the sharp interface limit as $\epsilon \rightarrow 0$, in [CL2], estimates based on the sub-mean value inequalities for sub-caloric functions have been derived. One may attempt to extend the derivations in [CL2] to the discrete case, but the details remain to be worked out.

3.2. A decoupled implicit nonlinear scheme

Scheme (15) requires the solution of a coupled nonlinear eigenvalue system. We now present an alternative which is similar to (15) in spirit but allows the decoupling between the different components. In the jargon of numerical methods, this can be viewed as a Gauss–Seidel version of (15).

$$\delta_t u_j^n = \Delta u_j^{n+1} + \lambda_j^n u_j^{n+1} - \frac{2}{\epsilon^2} \left(\sum_{i < j} (u_i^{n+1})^2 + \sum_{i > j} (u_i^n)^2 \right) u_j^{n+1}, \quad (23)$$

in $\Omega \times \mathbb{R}_+$, along with the boundary condition $u_j^{n+1} = 0$ on $\partial\Omega \times \mathbb{R}_+$, and the normalization condition (17).

A distinct feature of (23) is that, at each time step, the components of $\{u_j^{n+1}\}$ can be solved sequentially from $j = 1$ to m from a linear eigenvalue problem which is decoupled from the remaining unknown components.

Similar to lemma 3.1, scheme (23) can be related to the constrained variational problem:

$$\min \left\{ \int_{\Omega} \left(|\nabla u_j|^2 + 2F_{\epsilon}(\tilde{u}) + \frac{1}{\Delta t_n} |u_j - u_j^n|^2 \right) dx \mid u_j \in \bar{H}_0^1(\Omega) \right\}, \quad (24)$$

where \tilde{u} denotes the vector $(u_1^{n+1}, \dots, u_{j-1}^{n+1}, u_j, u_{j+1}^n, \dots, u_m^n)$.

The objective functional in (24) is a convex quadratic functional, so the existence and uniqueness are assured for any step size. The constraints lead to the norm-preserving property,

$$\int_{\Omega} |\tilde{u}_i^{n+1, j}|^2 dx = 1, \quad \forall i, j, n, \quad (25)$$

where the notation $\tilde{u}^{n+1, j} = (u_1^{n+1}, \dots, u_j^{n+1}, u_{j+1}^n, \dots, u_m^n)$ is used. From the variational formulation, we then have

$$\begin{aligned} E^{\epsilon}(\tilde{u}^{n+1, j}) + \frac{1}{\Delta t_n} \int_{\Omega} |\tilde{u}^{n+1, j} - u^n|^2 dx \\ \leq E^{\epsilon}(\tilde{u}^{n+1, j-1}) + \frac{1}{\Delta t_n} \int_{\Omega} |\tilde{u}^{n+1, j-1} - u^n|^2 dx, \quad \forall j. \end{aligned} \quad (26)$$

The energy decreasing property easily follows from the above by noticing that $u^n = \tilde{u}^{n+1,0}$ and $u^{n+1} = \tilde{u}^{n+1,m}$. Similar to lemma 3.3, the decoupled scheme also preserves the non-negativity of the solutions under suitable conditions on time steps. For the Lagrange multipliers (or the eigenvalues of the associated linear eigenvalue problem), the corresponding formula becomes

$$\lambda_j^{n+1} = \int_{\Omega} [|\nabla u_j^{n+1}|^2 + u_j^{n+1} F_{\epsilon,j}(\tilde{u}^{n+1,j})] \, d\mathbf{x} + \frac{1}{\Delta t_n} (1 - \int_{\Omega} u_j^{n+1} u_j^n \, d\mathbf{x}). \quad (27)$$

Convergence analysis of the decoupled scheme can be provided using the same line of argument as in the previous subsection. The details are omitted here.

3.3. An efficient semi-implicit operator splitting scheme

The implicit algorithms given earlier require the solution of either a coupled non-convex nonlinear eigenvalue problem or a set of decoupled linear eigenvalue problems. To avoid implementing nonlinear or eigen-problem solvers, it is natural to consider possible semi-implicit schemes through operator or time-splitting schemes which were widely used in the physical literature (see [BaD, BJM] for more references).

We now consider an operator splitting method which can be efficiently implemented to give a fully discrete numerical scheme whose solution complexity is linear with respect to the number of discrete unknowns. The method is essentially based on the splitting of the three terms in equation (4), namely, the diffusion term, the nonlinear interaction term and the Lagrange multiplier term. They can in turn be solved respectively by fast heat equation solver, direct ODE integration and a normalization. We start with the semi-discretization in time first and then consider implementing the spatial discretization.

The discrete in time operator splitting scheme is given as follows: given the solution $u^n = u^n(\mathbf{x})$ at the time level t_n , the solution for the next level t_{n+1} is computed in three steps:

Step 1: a heat equation solver:

$$\begin{cases} \frac{\partial u}{\partial t} = \Delta u, & \mathbf{x} \in \Omega, \, t_n < t < t_{n+1}, \\ u(t_n, \mathbf{x}) = 0, & \mathbf{x} \in \partial\Omega, \, t_n < t < t_{n+1}, \\ u(t_n, \mathbf{x}) = u^n(\mathbf{x}), & \mathbf{x} \in \Omega. \end{cases} \quad (28)$$

Set $\hat{u}^{n+1} = u(t_{n+1}, \mathbf{x})$ as the solution of (28) at $t = t_{n+1}$.

Step 2: a (Gauss–Seidel) solver of decoupled ODEs: sequentially for $j = 1, \dots, m$,

$$\begin{cases} \frac{\partial u_j}{\partial t} = -\frac{2u_j}{\epsilon^2} \left(\sum_{i<j} (\tilde{u}_i^{n+1})^2 + \sum_{i>j} (\hat{u}_i^{n+1})^2 \right), & \mathbf{x} \in \Omega, \, t_n < t < t_{n+1}, \\ u_j(t_n, \mathbf{x}) = \hat{u}_j^{n+1}(\mathbf{x}), & \mathbf{x} \in \Omega. \end{cases} \quad (29)$$

Set $\tilde{u}^{n+1} = u(t_{n+1}, \mathbf{x})$ as the solution of the above system at $t = t_{n+1}$.

Step 3: normalization, that is, get u^{n+1} via

$$u_j^{n+1} = \frac{\tilde{u}_j^{n+1}}{\|\tilde{u}_j^{n+1}\|}, \quad j = 1, \dots, m, \quad (30)$$

with $\|\cdot\|$ denoting the standard L^2 norm.

Some comments are now in order. We first note that (30) is equivalent to solving the ODE systems

$$\frac{\partial}{\partial t} u_j = -\bar{\lambda}_j(t) u_j, \quad j = 1, \dots, m, \quad (31)$$

with the initial condition $u_j(t_n, \mathbf{x}) = \tilde{u}^{n+1} = u(t_{n+1}, \mathbf{x})$ and a modified Lagrange multiplier $\bar{\lambda}_j$ satisfying

$$\int_{t_n}^{t_{n+1}} \bar{\lambda}_j(t) dt = \log(\|\tilde{u}^n\|),$$

which would ensure that the normalization condition (3) is satisfied by the solution of (31) at $t = t_{n+1}$; see similar discussions in [B, BaD].

In addition, the gradient flow (28) can be viewed as applying the steepest descent to the Dirichlet integral part of the energy E^ϵ without the constraint. Similarly, (29) can be viewed as a Gauss–Seidel based component-wise steepest descent of the potential energy part of the energy $E^\epsilon(u)$ without the constraint and the final step (30) projects the solution back to the constrained manifold (10) in order to satisfy (3).

From a computational point of view, equation (29) can be solved exactly by

$$\tilde{u}^{n+1} = \hat{u}_j^{n+1}(\mathbf{x}) \exp \left\{ -\frac{2\Delta t_n}{\epsilon^2} \left(\sum_{i<j} (\tilde{u}_i^{n+1})^2 + \sum_{i>j} (\hat{u}_i^{n+1})^2 \right) \right\}. \quad (32)$$

The gradient flows (28) can also be solved via many well-known techniques. In our numerical simulations (see discussions in the next section), an efficient implementation is carried out which has a computational complexity nearly linearly proportional to the number of discretization variables.

We note that each step of the splitting scheme again preserves the non-negativity of the solutions $\{u_j^n\}$. In fact, this holds true for any time step size.

Lemma 3.4. *The solution of the splitting scheme (28)–(29)–(30) satisfies for any $n \geq 1$ and any $j = 1, \dots, m$ that,*

$$u_j^n(\mathbf{x}) \geq 0, \quad \text{a.e. in } \Omega. \quad (33)$$

Proof. Note that for (28), the well-known maximum principle leads to the non-negativity. The explicit solution (32) assures the non-negativity for (29). Finally, the projection by the norm in (30) is certainly non-negativity preserving as well. Thus, the lemma can be proved with induction. \square

For sufficiently small Δt_n , the energy decreasing property can also be established similarly to the discussion given in [BaD], we leave detailed discussions to future work. We also note that while the time-splitting scheme can be effective for dynamic simulations, due to the splitting error, the time steps would have to be small for large time in order to get a good approximation of the equilibrium solution. Yet, should the equilibrium solution be the focus, alternative schemes can also be used, for example, the Gauss–Seidel type iterations studied in [CLLL], methods presented in earlier subsections and those discussed in [B, BaD].

4. Numerical simulations and applications

In this section, we present some studies that illustrate both the effectiveness of the numerical algorithms and the interesting features of the normalized gradient dynamics associated with the optimal eigenvalue partition problem.

In our simulations, the computational domain Ω is taken as a two dimensional box. Higher dimensional versions can also be readily implemented. For illustration purposes, instead of the homogeneous Dirichlet boundary condition $\partial\Omega$, a periodic boundary condition is used which

effectively makes the simulation as that for a periodic partition of the whole space. Much of the analysis remains valid with the periodic boundary condition.

The periodic boundary condition allows the spatial discretization of the Laplacian operator to be discretized by a Fourier spectral scheme via the FFT implementation. For suitably given aspect ratios, it is expected that the optimal partition would be given by the regular hexagons when the number of subdomains is suitably chosen, much like the honeycomb structure shown earlier. Meanwhile, other patterns may be expected when the number of subdomains and the aspect ratios of the computational domain do not allow a perfect hexagonal tiling, as demonstrated in the final numerical example. Some studies on the limiting subdomain shapes have been carried out [CL1] which reveals the preference of the hexagon like shapes when the number of subdomains approaches infinity.

Here, we are particularly interested in the subdomain partition which is governed implicitly by the evolution of the solutions $\{u_j^\epsilon(t, \mathbf{x})\}$ of the system (4). To better visualize the subdomain evolution, we assign an integer valued marker function $\chi(t, \mathbf{x})$ which takes on the value $\chi = i$ (to represent the subdomain Ω_i) in the region where u_i^ϵ dominates all the other $\{u_j^\epsilon\}_{j \neq i}$. Meanwhile, the effect of the diffuse interface approximation can be very well captured from the nonlinear interaction function F_ϵ given by (2) as well as its integral functional $S^\epsilon = S^\epsilon(u^\epsilon(t, \mathbf{x}))$ over the computational domain as defined by (14).

We also note that by (12) and the definition in (14), $\Lambda^\epsilon = \Lambda^\epsilon(u^\epsilon(t, \mathbf{x}))$ gives an estimate of the sum of the Lagrange multipliers. In the limit as $\epsilon \rightarrow 0$, $\Lambda^\epsilon = \Lambda^\epsilon(u^\epsilon(t, \mathbf{x}))$ also provides an estimate often more accurate than the energy $E^\epsilon = E^\epsilon(u^\epsilon(t, \mathbf{x}))$ to the sum of the principal eigenvalues associated with the subdomain partition.

4.1. Convergence test of the discretization

We first study the convergence of the discretization for the normalized gradient flow with a given $\epsilon > 0$. For illustration, we take $m = 4$ with the computational domain to be of the size $2\pi \times \sqrt{3}\pi$ so that the optimal partition is made up of four congruent regular hexagons with boundary edge of length $\pi/\sqrt{3}$.

With ϵ choosing as $5e-3=0.005$, we compute the numerical solutions with different grids and time steps and then evaluate the energy $E^\epsilon = E^\epsilon(u^\epsilon(t, \mathbf{x}))$ and the functional $S^\epsilon = S^\epsilon(u^\epsilon(t, \mathbf{x}))$, respectively. Note that with ϵ being fixed, $S^\epsilon = S^\epsilon(u^\epsilon(t, \mathbf{x}))$ remains substantially above zero. The time evolutions are shown in figure 3 with the different colours (from black to blue to green then to red for the online colour version, and from bottom to top for the printed version) representing spatial grids of sizes from 64×64 to 128×128 to 256×256 and to 512×512 (the higher resolution curves are also above those with lower resolutions in the plot). Within the same spatial grid, two different time steps are also used. For the coarsest spatial grid, the time steps are $8e-4$ (circles) and $1.6e-3$ (dots). We note that the differences between the plots get smaller and smaller with increasing resolution. As far as the energy plots are concerned, the doubling of time steps no longer makes any difference on the finer spatial grids (in green and red colours). Moreover, for the plots of $S^\epsilon = S^\epsilon(u^\epsilon(t, \mathbf{x}))$, we notice that the data based on the finer spatial grid with the larger time step nearly coincides with that on the grid of the next coarser level but with the time step being halved. While such an observation remains to be explored further, the convergence of the discrete approximation is clearly seen for the given value of ϵ .

4.2. Sharp interface limit

We now examine more carefully the effect of ϵ and consider the sharp interface limit of the numerical solutions to show that for small $\epsilon > 0$, the normalized gradient flows can offer

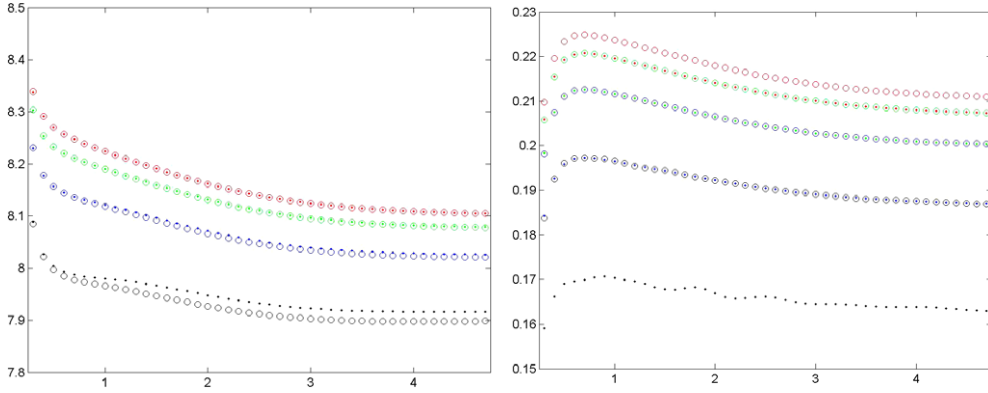


Figure 3. Approximations of E^ϵ and S^ϵ for $\epsilon = 5e - 3$. For the colour plots in the online version, each change of colour implies a doubling of spatial resolution and a halving of the time step size. For the same colour, the time steps used for the dotted lines are twice the steps used for the circles.

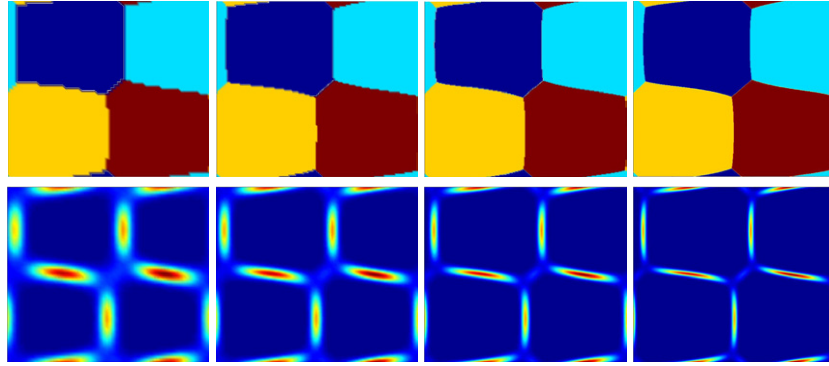


Figure 4. Sharp interface: subdomain partitions (top) and diffuse interface layers (bottom) at $t = 0.4$ for $\epsilon = 0.04, 0.02, 0.01$ and 0.005 computed with gradually increased resolution.

good approximations to the limiting behaviour as $\epsilon \rightarrow 0$. We again take $m = 4$ with the computational domain being of the size $2\pi \times \sqrt{3}\pi$.

Let λ^* be the smallest eigenvalues of the (negative) Laplacian on a unit regular hexagon, then using the estimate given in [CK] for λ^* and a simple scaling, it can be found that the sum of the corresponding principal eigenvalues on the four subdomains is $12\lambda^*/\pi^2 \approx 12 \times 7.155339/\pi^2$. We thus expect that in the sharp interface limit, the energy E^ϵ and estimate of the sum of the Lagrange multipliers would get close to $12\lambda^*/\pi^2$, which takes an approximate value of 8.699849 or roughly 8.7.

We first present some solutions computed with decreasing values of ϵ but increasing levels of resolution. The density plots in figures 4 and 5 correspond to the computed solutions at $t = 0.4$ and their long time asymptotic limit for the marker function χ and the nonlinear interaction function F_ϵ . Here, we take $\epsilon = 0.04, 0.02, 0.01$ and 0.005 . The computations are performed for $\epsilon = 0.04$ with a 64×64 grid and a time step $\Delta t_n = 8e - 4$ first, then for each halving of ϵ , we double the number of spatial grid points and halve the time step. The grids and time steps are refined to ensure that the resolution is sufficient for the corresponding values of ϵ . The pictures in figures 4 and 5 show good consistency of the subdomain partitions and good resolution of diffuse interfacial layers.

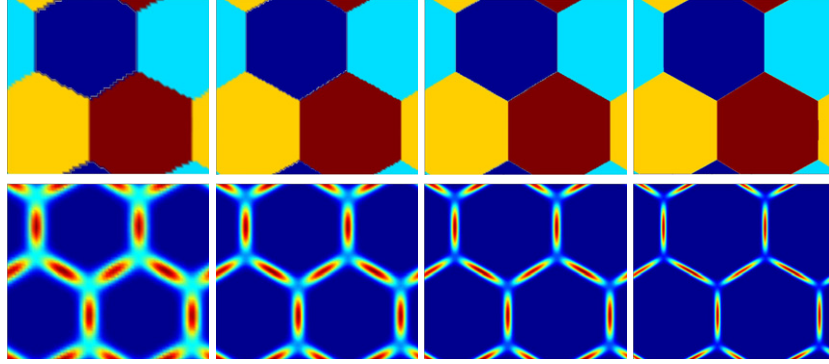


Figure 5. Sharp interface: subdomain partitions in the asymptotic time limit (top) and diffuse interface layers (bottom) for $\epsilon = 0.04, 0.02, 0.01$ and 0.005 computed with gradually increased resolution.

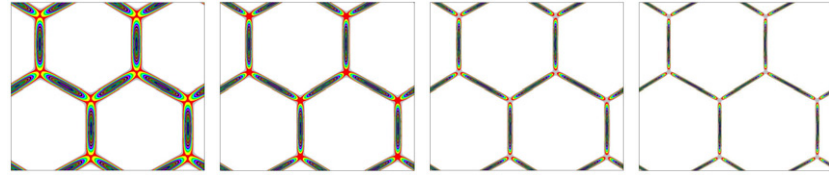


Figure 6. Sharp interface: the diffusion interfacial layer depicted by the asymptotic time limit of the nonlinear interaction term F_ϵ for $\epsilon = 0.01, 0.005, 0.0025$ and 0.00125 .

In figures 4 and 5, the diffuse interfacial layers depicted by the plots of F_ϵ also illustrate that as ϵ gets smaller, the interfacial regions start to get narrower as well. In figure 6, the plots of the long time limit of F_ϵ are again shown, for $\epsilon = 0.01, 0.005, 0.0025$ and 0.00125 , based on the numerical solutions on a fine grid of the size 1024×1024 with an exceedingly small time step size of $1e-6$. A close examination shows that the width of the interfacial layer is seen to be linearly proportional to the constant ϵ . Though this is a typical feature of diffuse interface models, more analytical characterizations of this observation remain to be carried out in the present context.

To offer a more precise characterization of the behaviour of the solutions in the sharp interface limit additional numerical results of several quantities are provided. These include the long time asymptotic limit Λ_*^ϵ of $\Lambda^\epsilon = \Lambda^\epsilon(u^\epsilon(t, \mathbf{x}))$ and the long time asymptotic limit S_*^ϵ of the integral $S^\epsilon = S^\epsilon(u^\epsilon(t, \mathbf{x}))$ defined in (14). In [CL2], it has been shown that the integral of $S^\epsilon = S^\epsilon(u^\epsilon(t, \mathbf{x}))$ over any finite time interval goes to zero like a power of ϵ as $\epsilon \rightarrow 0$, but no estimate on the precise exponent is given. In figure 7, the plot of $1 - \Lambda_*^\epsilon \pi^2 / (12\lambda^*)$ with respect to $1/\epsilon$ is present in the right figure for several decreasing values of ϵ . Clearly, as ϵ gets smaller, $1/\epsilon$ gets larger, $1 - \Lambda_*^\epsilon \pi^2 / (12\lambda^*)$, gradually decreases to zero, illustrating the convergence of Λ_*^ϵ to its sharp interface limit of $12\lambda^* / \pi^2$, which is the minimum sum of the principle eigenvalues with a partition with four subdomains. Meanwhile, the plot of S_*^ϵ with respect to a number of decreasing values of $\sqrt{\epsilon}$ is given in the left picture (red circles). The results seem to indicate that S_*^ϵ is nearly linear with respect to $\sqrt{\epsilon}$ based on the good agreement of the data points with its linear least square fit (the dash line). More precise analytical confirmation of such a dependence remains to be further studied.

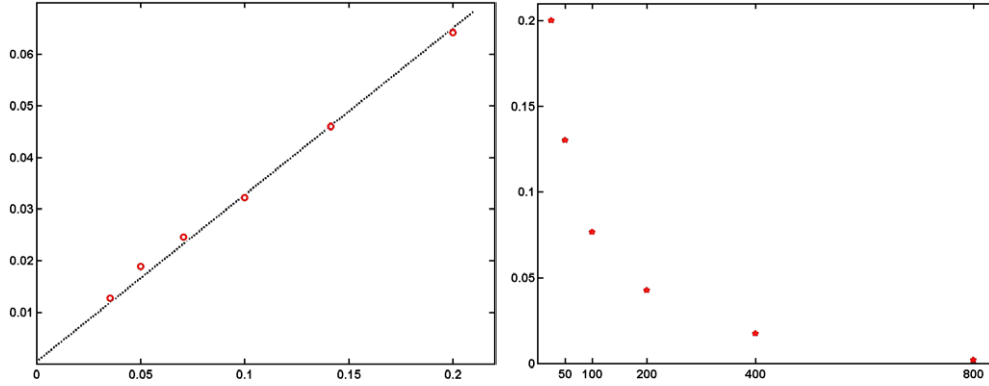


Figure 7. Convergence to the sharp interface limit: plot of S_ϵ^* against $\sqrt{\epsilon}$ (circles) along with its linear fit (dashed line), and plot of $1 - \Lambda_*^\epsilon \pi^2 / (12 \lambda_*^*)$ against $1/\epsilon$.

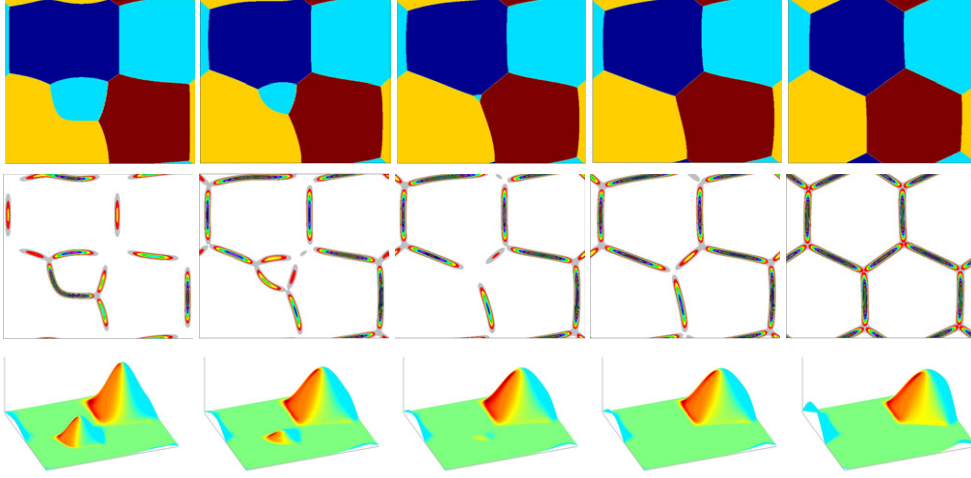


Figure 8. Partitions at $t = 0.1, 0.3, 0.4, 0.5$ and 3.0 (top), the interfacial layers between subdomains (middle), and the component undergoing the topological change (bottom).

4.3. Topological changes in the interfacial dynamics

We again take $m = 4$ with the computational domain of the size $2\pi \times \sqrt{3}\pi$ similarly to the previous examples. We however take one of the initial subdomains to be disconnected (see the left picture in figure 8). As time goes on, one of the disconnected components starts to shrink and eventually disappears so that each of the four subdomains stays as a single connected domain, the final partition then becomes the same as that shown in the previous examples. The evolution and the topological changes are illustrated in figure 8 through the density plots of the marker functions and the nonlinear interaction functions (for the interfacial layers). To highlight the evolution of the solution component that corresponds to the specific subdomain undergoing the topological changes, we also provide the surface plots of the particular solution component which has two regions of non-overlapping support initially with one of the regions eventually vanishing around $t = 0.4$.

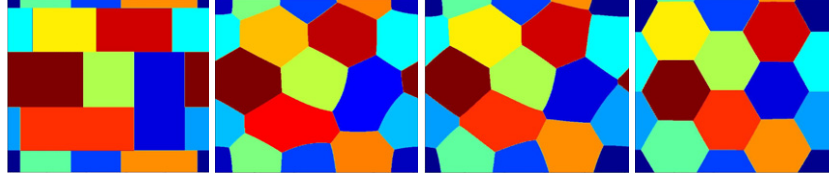


Figure 9. A 12-subdomain partition: initial partition (left) and subdomains at times $t = 0.1, 2.4$ and 10.

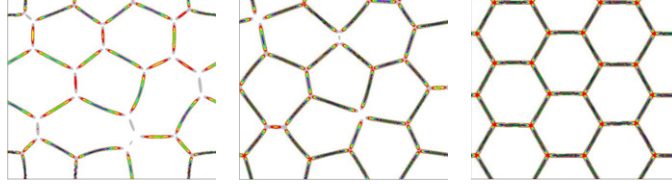


Figure 10. A 12-subdomain partition: interfacial layers between subdomains at times $t = 0.1, 2.4$ and 10.

4.4. Time scales in the interfacial dynamics

We now present an example with $m = 12$ and the domain of size $2\pi \times \sqrt{3}\pi$. Since the computational domain can be equally partitioned into three smaller domains each of size $2/\sqrt{3}\pi \times \sqrt{3}\pi$ by a simple scaling argument, each of the smaller domains allows an optimal periodic partition into 4 regular hexagonal domains. We thus expect to see a periodic copy of the similar patterns as given in the earlier examples with $m = 4$ except by a 90° rotation. In figures 9 and 10, the marker function χ and the nonlinear interaction function F_ϵ are again plotted at different time instances respectively.

We observe that while the initial subdomains are all of rectangular type, the subdomains transform quickly via the formation of a number of triple junctions. Even at very early stages of the time evolution, the triple junctions consist of interfaces intersecting at equal angles ($2\pi/3$). The interfaces (as the limit of the interfacial layer or that defined by the marker function) also start to become nearly straight line segments connecting the triple points during the early transient dynamics. Afterwards, a much slower transition to the hexagonal partition patterns begins to take place. The equal angle properties and the behaviour of the interface during the different stages of the time evolution are remarkably similar to the well-known properties of two dimensional grain growth in a homogeneous elastic media with constant surface tension. Analytically, they are also related to the theoretical studies of the nodal sets of the vector-valued maps [CL, L, LY, St, SV]. These computational results again motivate further analytical studies of the scaling behaviour of the time evolution governed by the normalized gradient flow and to make connections between the interfacial motion governed by both surface energies and bulk energies.

4.5. Multiple steady state configurations

As the final example, we demonstrate the existence of multiple local minimizers for the energy functional E^ϵ constrained by the normalization condition. We simply take a computational domain in the form of a unit square. Again a periodic boundary condition is imposed. By setting $m = 5$ and using a few different initial conditions shown in figure 11, their respective

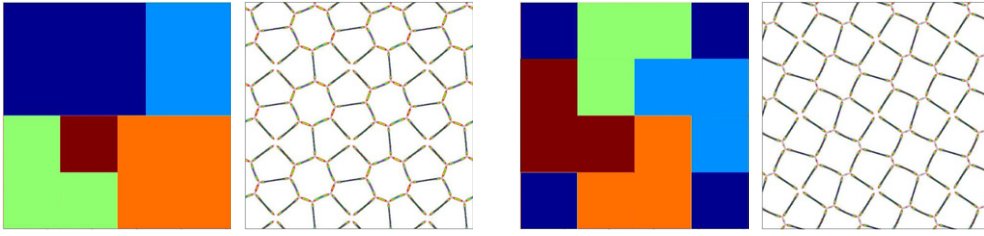


Figure 11. Locally optimal partitions: marker functions of two different initial conditions and diffuse layers showing the periodic extensions of their long time limits.

long time asymptotic limits are computed. The final limiting solutions are also numerically tested to be stable under small random perturbations. In order to better visualize the resulting partition patterns, we periodically extend the final limiting solutions by two extra periods in both coordinate directions and present the density plot of the nonlinear interaction term F_ϵ to highlight the diffuse interface layer. That implies the computational domain showing the initial condition with five subdomains is actually one-ninth of the domain showing the final limiting solutions with 45 subdomains (under the periodic condition). These partition patterns are obviously not optimal, but they reveal the existence of many possible local minimizers of the energy and thus demonstrate the complex energy landscape subject to the normalization constraints. Such minimizers still persist even with diminishing ϵ . It remains to be studied further how to characterize the global minimizers for the partition of general domains into a generic number of subdomains.

5. Conclusions

In this paper, the numerical approximation of a norm-preserving gradient flow is considered along with the study of the nonlinear interfacial dynamic related to a non-local eigenvalue optimal partition problem. Both spatial and time discretizations are discussed with particular emphasis on preserving the properties shared by the continuous counterpart and the efficient implementation. Numerical analysis is performed and computational examples are provided. Interesting features of the nonlinear dynamics governed by the normalized gradient flow are illustrated, such as the changes in subdomain topology, the changes in the dynamics at different time scales, and the complex energy landscape. Some analysis on the effect of the diffuse interface relaxation is also made. These observations also serve as motivations for further analytical and computational studies of the physically more complex interfacial motion governed by both the surface energies and the bulk energies.

While the examples presented here are limited to two dimensional settings, extensions to higher dimensional cases are straightforward. Due to the use of periodic conditions, the boundary effect is not examined. Also, for cases with an exceedingly large number of subdomains, more compact approximation schemes may be developed. Comparisons with other schemes such as the ones in [B, BaD, CLLL] may also be conducted for equilibrium computations. We leave these and other issues to future investigations.

Acknowledgments

The research of Du is supported in part by NSF DMS-0712744 and NIH CA125707. The research of Lin is supported in part by NSF DMS-0700517. The authors would like to dedicate

this work to Professor Todd Dupont who provided great inspiration and guidance as a faculty mentor of Du when Du was a Dickson instructor at the University of Chicago from 1988 to 1990. F-H Lin was also a former colleague of Todd Dupont when he was a professor in the mathematics department during the same period.

References

- [AD] Aftalion A and Du Q 2001 Vortices in a rotating Bose–Einstein condensate: critical angular velocities and energy diagrams in the Thomas–Fermi regime *Phys. Rev. A* **64** 063603
- [B] Bao W 2004 Ground states and dynamics of multi-component Bose–Einstein condensates *SIAM MMS* **2** 210–36
- [BaD] Bao W and Du Q 2004 Computing the ground state solution of Bose–Einstein condensates by a normalized gradient flow *SIAM J. Sci. Comput.* **25** 1674–97
- [BJM] Bao W, Jin S and Markowich P A 2002 On time-splitting spectral approximations for the Schrödinger equation in the semiclassical regime *J. Comput. Phys.* **175** 487–524
- [BBW] Bernoff A, Bertozzi A and Witelski T 1998 Axisymmetric surface diffusion: dynamics and stability of self-similar pinchoff *J. Stat. Phys.* **93** 725–76
- [BDa] Buttazzo G and Dal Maso G 1991 Shape optimization for Dirichlet problems: relaxed formulation and optimality conditions *Appl. Math. Optim.* **23** 17–49
- [CL] Cafferelli L and Lin F H 2008 Singularly perturbed elliptic systems and multi-valued harmonic functions with free boundaries *J. Am. Math. Soc.* **21** 847–862
- [CL1] Cafferelli L and Lin F H 2007 An optimal partition problem for eigenvalues *J. Sci. Comput.* **31** 5–18
- [CL2] Cafferelli L and Lin F-H 2009 Nonlocal heat flows preserving the L^2 energy *Discrete Contin. Dyn. Syst.* **23** 49–64
- [CLLL] Chang S-M, Lin C-S, Lin T-C and Lin W-W 2004 Segregated nodal domains of two-dimensional multispecies Bose–Einstein condensates *Physica D* **196** 341–61
- [C] Chen L Q 2002 Phase-field models for microstructure evolution *Annu. Rev. Mater. Sci.* **32** 113–40
- [CTV1] Conti M, Terracini S and Verzini G 2002 Nehari’s problem and competing species systems *Ann. Inst. Henri. Poincaré Anal. Non Linéaire* **19** 871–88
- [CTV2] Conti M, Terracini S and Verzini G 2003 An optimal partition problem related to nonlinear eigenvalues *J. Funct. Anal.* **198** 160–96
- [CTV3] Conti M, Terracini S and Verzini G 2005 Asymptotic estimates for the spatial segregation of competitive systems *Adv. Math.* **195** 524–60
- [CTV4] Conti M, Terracini S and Verzini G 2005 A variational problem for the spatial segregation of reaction–diffusion systems *Indiana Univ. Math. J.* **54** 779–815
- [CK] Cureton L and Kuttler J 1999 Eigenvalues of the laplacian on regular polygons and polygons resulting from their dissection *J. Sound Vib.* **220** 83–98
- [D] Du Q 2002 Numerical computations of quantized vortices in Bose–Einstein condensate *Recent Progress in Computational and Applied PDEs* ed T Chan *et al* (Dordrecht: Kluwer) pp 155–68
- [D2] Du Q 1994 Finite element methods for the time-dependent Ginzburg–Landau model of superconductivity *Comput. Math. Appl.* **27** 119–33
- [DFG] Du Q, Faber V and Gunzburger M 1999 Centroidal Voronoi tessellations: applications and algorithms *SIAM Rev.* **41** 637–76
- [DLRW] Du Q, Liu C, Ryham R and Wang X 2005 A phase field formulation of the Willmore problem *Nonlinearity* **18** 1249–67
- [DLW] Du Q, Liu C and Wang X 2004 A phase field approach in the numerical study of the elastic bending energy for vesicle membranes *J. Comput. Phys.* **198** 450–68
- [L] Lin F-H 1991 Nodal sets of solutions of elliptic and parabolic equations *CPAM* **44** 287–306
- [LY] Lin F-H and Yang X-P 2002 *Geometric Measure Theory, An Introduction (Advanced Mathematics I)* (Boston, MA: International Press)
- [St] Struwe M 1988 On the evolution of harmonic maps in higher dimensions *J. Diff. Geom.* **28** 485–502
- [SV] Šverák V 1993 On optimal shape design *J. Math. Pures Appl.* **72** 537–51
- [YHCD] Yu P, Hu S, Chen L-Q and Du Q 2005 An iterative-perturbation scheme for treating inhomogeneous elasticity in phase-field models *J. Comput. Phys.* **208** 34–50
- [ZCD] Zhang L, Chen L-Q and Du Q 2007 Morphology of critical nuclei in solid state phase transformations *Phys. Rev. Lett.* **98** 265703